

"© 2016 IEEE. Personal use of this material is permitted. Permission from IEEE must be obtained for all other uses, in any current or future media, including reprinting/republishing this material for advertising or promotional purposes, creating new collective works, for resale or redistribution to servers or lists, or reuse of any copyrighted component of this work in other works."

Magnetic Field and Force Calculation in Linear Permanent-Magnet Synchronous Machines Accounting for Longitudinal End Effect

H. Z. Hu, J. Zhao, X. D. Liu, and Y. G. Guo

Abstract—This paper presents an improved analytical method for predicting the magnetic field and forces in linear permanent magnet synchronous machines (LPMSMs) accounting for both the primary end effect and secondary end effect. So far, the magnetic field calculation of LPMSM in most studies is conducted in Cartesian coordinate, whereas the end effect is neglected by applying periodic boundary. In this paper, to implement the analytical model, a polar presentation of the machine geometry is proposed and subdomain method is applied to calculate the magnetic field. Then, according to the developed model, the tangential thrust and normal force are calculated based on Maxwell stress theory. Numerical result is subsequently obtained by finite element method and employed to validate the analytical model. Finally, an LPMSM prototype is manufactured and experiments are conducted. The results show that the developed analytical model has high accuracy for predicting the magnetic field and forces.

Index Terms—Linear PM machines, improved analytical model, magnetic field, force.

I. INTRODUCTION

LINEAR permanent magnet (PM) synchronous machines (LPMSMs), which can provide thrust force directly to a payload, are being employed increasingly in the commercial, industrial, and military products benefiting from the high force density, efficiency, dynamic performance, positioning accuracy, and no mechanical transmission [1-6]. Different from the conventional rotary machines, LPMSMs suffer from end effect due to the finite length of the primary part and the secondary part, which makes the magnetic field be distorted seriously at the longitudinal ends and induces serious torque ripple [7]. In the design of PM machines, an accurate prediction of the magnetic field distribution has an important significance for the performance analysis, dynamic modeling and parameter optimization [6], [9].

Many numerical and analytical methods have been employed to analyze the magnetic field of LPMSM, such as finite element method (FEM) [2], [9]-[14], magnetic equivalent circuit (MEC) method [6]-[7], [14]-[19], subdomain method (SD) [2], [4], [13], [20]-[25] and hybrid method [14], [26]. Each method has its own strength and pitfall. FEM is regarded as the most accurate tool as it can take saturation into consideration and almost no simplification of the actual geometry is needed, but it is still relatively time-consuming and cannot provide physical insight into the relationship between design parameters and

machine performance. The analytical methods are still preferred in the stages of preliminary design and optimization. The MEC method is widely used due to its simplicity and that it can account for magnetic saturation, curvature and fringing effect. However, it can only calculate the magnetic field at a few discrete points of the structure and lacks adequate accuracy, particularly when the flux leakage is significant. The analytical model based on subdomain method can provide more accurate prediction of magnetic field distribution and it is increasingly used in various PM machines.

In many analytical models, the magnetic field is calculated on the assumption that the length of LPMSM is infinite or periodic boundaries are added to the machine. Thus, the longitude end effects can be excluded. For example, the magnetic fields of slotless LPMSM [2] and double-sided air-core LPMSM [20] are calculated and the electromagnetic thrust force is analyzed by assuming that each layer is infinite in the x -axis direction. In [4], the magnetic field of LPMSM with stair-step-shaped magnetic poles is calculated by using the SD method and superposition theorem by extending the length of machine to infinite. On the same assumption, a general framework for the calculation of open-circuit and armature reaction magnetic field distribution of slotless tubular LPMSM [21] and slotted tubular LPMSM [22] is presented. The assumption of infinite length or adding periodic boundary conditions apparently simplifies the formulation procedure. However, the primary end effect and the secondary end effect are both ignored, and the modeling precision is also reduced, which unavoidably influences subsequent system design and motion control implementation of electric machines.

In order to consider the end effect, some analytical models are established and applied to LPMSM. In [7], [16]-[17], [19], the longitude end effect is considered by MEC method and there is a relatively large error compared with FEM. In [23], the armature reaction field in move-coils PMLSM with finite motor length is calculated by analytical model based on harmonic expansion and permeance model. In [24], to consider the primary end effect, an enlarged slot is added to the end of iron yoke and then periodic boundary is imposed. However, only the primary end effect can be approximated and the secondary end effect is ignored. In [27], a Schwarz-Christoffel (SC) mapping-based method is presented for predicting the thrust force of permanent magnet linear motors (PMLMs) with accounting for slotting effect and end effect.

In this paper, an exact SD model which can consider both the primary end effect and secondary end effect is proposed. In this analytical model, the LPMSM is firstly deformed into an arc-segment linear PM machine instead of directly calculating

the magnetic field in Cartesian coordinates. The analytical model may have different radius of curvature. Then the magnetic field is calculated by SD model in polar coordinates and validated by FEM with the actual model. The thrust force and normal force are further investigated which can benefit performance optimization and dynamic modeling of LPMSM. A research prototype with slotless iron core is developed, and experiments are conducted to verify the developed analytical model.

II. THE MODEL OF LPMSM

Fig. 1(a) illustrates the analytical model of LPMSM in Cartesian coordinates without considering the slot effect. The parameters in LPMSM are: the length of the primary iron, L_s , the height of the primary iron, h_s , the length of the secondary back-iron, L_r , the height of the secondary back-iron, h_r , pole pitch, L_p , the width of PMs, L_m , the height of the PMs, h_m , the length of air-gap, g , and the length of the analytical model in Cartesian coordinates, L_{re} . It can be seen that if the primary end effect and secondary end effect are both considered, the magnetic field should be divided into 10 subdomains: 1, 2-1, 2-2, 3-1, ..., 6, and the length of the analytical model L_{re} is infinite. The large number of subdomains will introduce many boundary and interface conditions, which make the field calculation very complicated.

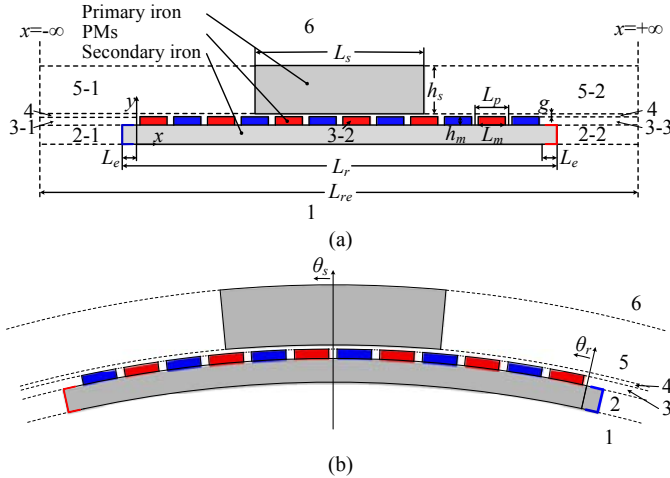


Fig. 1. The analysis model for LPMSM. (a) The analytical model in Cartesian coordinates; (b) The approximate analytical model in polar coordinates.

In order to reduce the number of subdomains, an approximate analytical model is proposed and Fig. 1(b) shows how the approximate analytical model is developed for slotless LPMSM. The left subdomains 2-1, 3-1, and 5-1 extend to the left boundary $x=-\infty$ and the right subdomains 2-2, 3-3, and 5-2 extend to the right boundary $x=+\infty$. Considering the symmetry, the LPMSM is deflexed to make the left boundary $x=-\infty$ and the right boundary $x=+\infty$ connect together, and the subdomains 2-1 and 2-2, 3-1, 3-2 and 3-3, 5-1 and 5-2 are combined to subdomain 2, 3, 5, respectively. The analytical model of LPMSM in Cartesian coordinates is converted to an arc-segment PMSM with the radius of curvature $r \rightarrow +\infty$. If the length of the analytical model in Cartesian coordinates L_{re} is a finite value, the radius of the approximate analytical model in polar coordinates r will also be a finite value and the

approximate analytical model will be obtained. The only difference between the analytical model in Cartesian coordinates and the approximate analytical model in polar coordinates is the influence of curvature. In the approximate analytical model, the secondary back-iron and PMs are converted to the arc rotor of a conventional rotary PMSM, and the primary iron is converted to an arc stator. The magnetization direction of PMs is changed from the y -direction in Cartesian coordinates to the radial direction in polar coordinates. Comparing with the analytical model in Cartesian coordinates, the number of subdomains in the approximate analytical model is reduced from 10 to 6. In the model shown in Fig. 1(b), both the primary end effect and secondary end effect can be considered. The secondary end effect is mainly caused by the interaction between the PMs and the primary iron when the primary part moves to the end of the secondary part. The extension of the secondary back-iron has little influence on the magnetic field distribution and force characteristic. Hence, to further reduce the number of subdomains, the secondary back-iron is extended and rolled into a ring, as shown in Fig. 2. In this model, the subdomains 1, 2 in Fig. 1 (b) have disappeared and the subdomains 3, 4, 5, 6 in Fig. 1 (b) are converted to 1, 2, 3, and 4. Meanwhile, it also should be noted that the analytical models with different radius of curvature can be obtained when different L_{re} is selected. When L_{re} is sufficiently large, the approximate analytical model in polar coordinates can be equivalent to the original LPMSM in Cartesian coordinates.

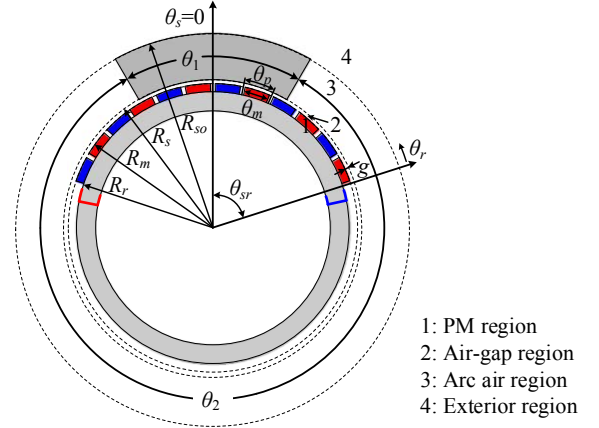


Fig. 2. The analytical model of LPMSM with extended secondary back-iron.

As shown in Fig. 2, the field domain is divided into four subdomains: 1) Region 1 is the PM region; 2) Region 2 is the air-gap region; 3) Region 3 is the arc air region; 4) Region 4 is the exterior region. The parameters in the analytical model are: inner radius of primary iron, R_s , outer radius of primary iron, R_{so} , outer radius of PM, R_m , outer radius of secondary back-iron, R_r , span angle of primary iron, θ_1 , span angle of Region 3, θ_2 , pole pitch, θ_p , span angle of PM, θ_m , and length of air-gap, g . To ensure that the magnetic field of LPMSM can be precisely calculated, the parameters of analytical models should be properly chosen. In the LPMSM, the position relationship between the primary iron and PMs, and the air-gap length are sensitive parameters and they should remain unchanged. Hence, R_m and θ_1 are firstly determined by:

$$R_m = \frac{L_{re}}{2\pi} \quad (1)$$

$$\theta_1 = \frac{L_s}{L_{re}} \times 2\pi \quad (2)$$

Then, the other parameters can be obtained as

$$R_s = R_m + g \quad (3)$$

$$R_{so} = R_m + g + h_s \quad (4)$$

$$R_r = R_m - h_m \quad (5)$$

$$\theta_p = \frac{L_p}{L_{re}} \times 2\pi \quad (6)$$

$$\theta_m = \frac{L_m}{L_{re}} \times 2\pi \quad (7)$$

III. ANALYTICAL SOLUTION OF MAGNETIC FIELD

In this paper, the following assumptions are made to enable and simplify the analytical solution: 1) The permeability of primary iron and secondary back-iron are infinite; 2) Axial end effect is negligible; 3) The relative permeability of gaps between magnets is assumed to be equal to that of PMs.

A. Model of the PMs

For arc-linear PMSM in polar coordinate, θ_s is the mechanical angular position in the stator reference frame ($\theta_s=0$ is the center of the primary iron) and θ_r is the mechanical angular position in the rotor reference frame ($\theta_r=0$ is the beginning of the PMs when pole arc to pole pitch ratio $\alpha_p=1$).

In polar coordinates, the magnetization vector \vec{M} of a PM can be given by

$$\vec{M} = M_r \vec{e}_r + M_\theta \vec{e}_\theta \quad (8)$$

where M_r is the radial component of the magnetization vector and M_θ is the tangential component. \vec{e}_r and \vec{e}_θ are the radial and tangential unit vectors, respectively. For radial magnetization, the waveforms of radial and tangential components are shown in Fig. 3.

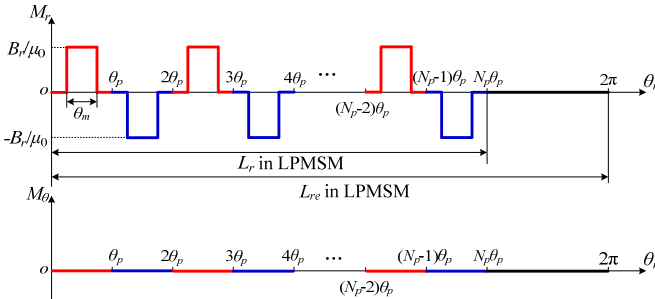


Fig. 3. Waveforms of the radial and tangential components of PM magnetization.

The radial and tangential components of the magnetization \vec{M} of each magnet can be expanded as Fourier series in the rotor reference frame, i.e.,

$$M_{ri}^r(\theta_r) = M_{ri0} + \sum_{n=1}^{\infty} [M_{ricn} \cos(n\theta_r) + M_{risn} \sin(n\theta_r)] \quad (9)$$

$$M_{\theta i}^r(\theta_r) = M_{\theta i0} + \sum_{n=1}^{\infty} [M_{\theta icn} \cos(n\theta_r) + M_{\theta isn} \sin(n\theta_r)]$$

Then the total radial and tangential components can be represented as

$$M_r^r(\theta_r) = \sum_{i=1}^{N_p} M_{ri}^r(\theta_r) \quad \text{and} \quad M_\theta^r(\theta_r) = \sum_{i=1}^{N_p} M_{\theta i}^r(\theta_r) \quad (10)$$

If the PMs rotate by $\theta_{sr} = \omega_r t + \theta_0$, where ω_r is the rotor rotational speed, and θ_0 is the initial position, the radial and tangential components can be represented in the stator reference frame through $\theta_s = \theta_r + \theta_{sr}$ as

$$M_r(\theta_s) = M_r^r(\theta_s - \theta_{sr}) = \sum_{n=1}^{\infty} [M_{rcn} \cos(n\theta_s) + M_{rsn} \sin(n\theta_s)] \quad (11)$$

$$M_\theta(\theta_s) = M_\theta^r(\theta_s - \theta_{sr}) = \sum_{n=1}^{\infty} [M_{\theta cn} \cos(n\theta_s) + M_{\theta sn} \sin(n\theta_s)] \quad (12)$$

B. Governing Partial Differential Equations

To describe the magnetic flux density \vec{B} , the magnetic vector potential \vec{A} is introduced. For the 2-D case in polar coordinates, the magnetic vector potential reduces to its axial component A_z . The governing equation is Poisson equation in Region 1 and Laplace equation in Regions 2, 3 and 4, i.e.,

$$\frac{\partial^2 A_{z1}}{\partial r^2} + \frac{1}{r} \frac{\partial A_{z1}}{\partial r} + \frac{1}{r^2} \frac{\partial^2 A_{z1}}{\partial \theta^2} = -\frac{\mu_0}{r} \left(M_\theta - \frac{\partial M_r}{\partial \theta} \right) \quad \text{in PM Region} \quad (13)$$

$$\frac{\partial^2 A_{zi}}{\partial r^2} + \frac{1}{r} \frac{\partial A_{zi}}{\partial r} + \frac{1}{r^2} \frac{\partial^2 A_{zi}}{\partial \theta^2} = 0 \quad i = \{2, 3, 4\} \quad (14)$$

The radial and tangential components of the flux density can be obtained from the vector potential distribution by

$$B_r = \frac{1}{r} \frac{\partial A_z}{\partial \theta} \quad \text{and} \quad B_\theta = -\frac{\partial A_z}{\partial r} \quad (15)$$

The general solutions of the vector potential in different subdomains are determined by using the Fourier series and the variable separation method.

1) In Region 1

By the variable separation method, the general solution of Poisson equation in PM region can be obtained by [28]

$$A_{z1}(r, \theta_s) = A_p(r, \theta_s) + \sum_{n=1}^{\infty} \left[A_{1n} \left(\frac{r}{R_m} \right)^n + B_{1n} \left(\frac{r}{R_r} \right)^{-n} \right] \cos(n\theta_s) + \sum_{n=1}^{\infty} \left[C_{1n} \left(\frac{r}{R_m} \right)^n + D_{1n} \left(\frac{r}{R_r} \right)^{-n} \right] \sin(n\theta_s) \quad (16)$$

where $A_p(r, \theta_s)$ is a particular solution of Poisson equation,

$$A_p(r, \theta_s) = \sum_{n=1}^{\infty} l_n(r) \cos(n\theta_s) + k_n(r) \sin(n\theta_s)$$

$$l_n(r) = \begin{cases} \frac{\mu_0 (M_{\theta cn} - nM_{rsn})}{n^2 - 1} r & n \neq 1 \\ -\frac{\mu_0 (M_{\theta cn} - M_{rsn})}{2} r \ln r & n = 1 \end{cases}$$

$$k_n(r) = \begin{cases} \frac{\mu_0 (M_{\theta sn} + nM_{rcn})}{n^2 - 1} r & n \neq 1 \\ -\frac{\mu_0 (M_{\theta sn} + M_{rcn})}{2} r \ln r & n = 1 \end{cases}$$

Applying the boundary condition on the surface of secondary back-iron which requires

$$H_{\theta 1} \Big|_{r=R_r} = -\frac{1}{\mu_0 \mu_r} \frac{\partial A_{z1}}{\partial r} - \frac{1}{\mu_r} M_\theta = 0 \quad (17)$$

the following equations can be obtained

$$A_{z1} = \sum_{n=1}^{\infty} \left[A_{1n} f_{1n}(r) + f_{1cn}(r) M_{\theta_{cn}} - f_{1sn}(r) M_{rsn} \right] \cos(n\theta_s) \\ + \sum_{n=1}^{\infty} \left[C_{1n} f_{1n}(r) + f_{1cn}(r) M_{\theta_{sn}} + f_{1sn}(r) M_{rcn} \right] \sin(n\theta_s) \quad (18)$$

where

$$f_{1n}(r) = \left(\frac{r}{R_m} \right)^n + \left(\frac{R_r}{R_m} \right)^n \left(\frac{r}{R_r} \right)^{-n} \\ f_{1cn}(r) = \begin{cases} \frac{\mu_0}{n^2-1} \left[nR_r \left(\frac{r}{R_r} \right)^{-n} + r \right] & n \neq 1 \\ \frac{\mu_0}{2} \left[R_r (1 - \ln R_r) \left(\frac{r}{R_r} \right)^{-1} - r \ln r \right] & n = 1 \end{cases} \\ f_{1sn}(r) = \begin{cases} \frac{\mu_0}{n^2-1} \left[R_r \left(\frac{r}{R_r} \right)^{-n} + nr \right] & n \neq 1 \\ -\frac{\mu_0}{2} \left[R_r (1 + \ln R_r) \left(\frac{r}{R_r} \right)^{-1} + r \ln r \right] & n = 1 \end{cases}$$

2) In Region 2

The general solution of Laplace equation in air-gap region is

$$A_{z2} = \sum_{n=1}^{\infty} \left[A_{2n} \left(\frac{r}{R_s} \right)^n + B_{2n} \left(\frac{r}{R_m} \right)^{-n} \right] \cos(n\theta_s) \\ + \sum_{n=1}^{\infty} \left[C_{2n} \left(\frac{r}{R_s} \right)^n + D_{2n} \left(\frac{r}{R_m} \right)^{-n} \right] \sin(n\theta_s) \quad (19)$$

3) In Region 3

The arc length of region 3 is θ_2 instead of 2π . Hence, the general solution of Laplace equation is different from that in regions 2 and 4. By the variable separation method, the general solution is

$$A_{z3} = \sum_{m=1}^{\infty} \left[a_{3m} \left(\frac{r}{R_{so}} \right)^{\lambda} + b_{3m} \left(\frac{r}{R_s} \right)^{-\lambda} \right] \\ \times \left[c_{3m} \cos \lambda \left(\theta_s + \frac{\theta_2}{2} - \pi \right) + d_{3m} \sin \lambda \left(\theta_s + \frac{\theta_2}{2} - \pi \right) \right] \quad (20)$$

where λ is the separation constant. By applying the boundary condition on the stator lateral surface of infinite permeability where the circumferential component flux density should be zero

$$B_{r3} \Big|_{\theta_s = \pi \pm \frac{\theta_2}{2}} = 0 \quad r \in (R_s, R_{so}) \quad (21)$$

the following equations can be obtained

$$\begin{cases} d_{3m} = 0 \\ \lambda = \frac{m\pi}{\theta_2} \end{cases} \quad (22)$$

Then, equation (20) can be rewritten as

$$A_{z3} = \sum_{m=1}^{\infty} \left[A_{3m} \left(\frac{r}{R_{so}} \right)^{\frac{m\pi}{\theta_2}} + B_{3m} \left(\frac{r}{R_s} \right)^{-\frac{m\pi}{\theta_2}} \right] \cos \frac{m\pi}{\theta_2} \left(\theta_s + \frac{\theta_2}{2} - \pi \right) \quad (23)$$

4) In Region 4

The general solution of Laplace equation in region 4 is

$$A_{z4} = \sum_{n=1}^{\infty} \left[(a_{4n} r^n + b_{4n} r^{-n}) \cos(n\theta_s) + (c_{4n} r^n + d_{4n} r^{-n}) \sin(n\theta_s) \right] \quad (24)$$

For region 4, the vector potential should be a finite value when the radius tends to the infinity:

$$|A_{z4}|_{r \rightarrow \infty} < \infty \quad (25)$$

Hence, the integration constants $a_{4n}=0$, $c_{4n}=0$. The vector potential in Region 4 can be rewritten as

$$A_{z4} = \sum_{n=1}^{\infty} \left[B_{4n} \left(\frac{r}{R_{so}} \right)^{-n} \cos(n\theta_s) + D_{4n} \left(\frac{r}{R_{so}} \right)^{-n} \sin(n\theta_s) \right] \quad (26)$$

C. Determination of Integration Constants

The coefficients A_{1n} , B_{1n} , $C_{1n} \sim D_{4n}$ are determined by applying the boundary and interface conditions, which are defined by the continuity of the normal flux density B_r and tangential field strength H_θ . It can be observed that some boundary conditions have been satisfied in the expressions of vector potential in (17), (21) and (25). The rest interface conditions between the subdomains are

$$r = R_m: \quad B_{r1} = B_{r2} \quad \forall \theta_s \quad (27)$$

$$r = R_m: \quad H_{\theta 1} = H_{\theta 2} \quad \forall \theta_s \quad (28)$$

$$r = R_s: \quad B_{r2} = B_{r3} \quad \text{or} \quad A_{z2} = A_{z3} \quad \theta_s \in \left(\pi - \frac{\theta_2}{2}, \pi + \frac{\theta_2}{2} \right) \quad (29)$$

$$r = R_s: \quad H_{\theta 2} = \begin{cases} H_{\theta 3} & \theta_s \in \left(\pi - \frac{\theta_2}{2}, \pi + \frac{\theta_2}{2} \right) \\ 0 & \text{otherwise} \end{cases} \quad (30)$$

$$r = R_{so}: \quad B_{r4} = B_{r3} \quad \text{or} \quad A_{z4} = A_{z3} \quad \theta_s \in \left(\pi - \frac{\theta_2}{2}, \pi + \frac{\theta_2}{2} \right) \quad (31)$$

$$r = R_{so}: \quad H_{\theta 4} = \begin{cases} H_{\theta 3} & \theta_s \in \left(\pi - \frac{\theta_2}{2}, \pi + \frac{\theta_2}{2} \right) \\ 0 & \text{otherwise} \end{cases} \quad (32)$$

By applying the rest interface conditions, the following linear equations are obtained

$$\begin{bmatrix} \mathbf{K}_1 & \mathbf{K}_2 & -\mathbf{I} & \mathbf{0} \\ \mathbf{K}_3 & \mathbf{K}_2 & \mathbf{I} & \mathbf{0} \\ \mathbf{0} & \mathbf{K}_4 & \mathbf{K}_5 & \mathbf{0} & \mathbf{0} & \mathbf{0} & \mathbf{K}_6 & \mathbf{K}_7 & \mathbf{0} & \mathbf{0} \\ \mathbf{0} & \mathbf{0} & \mathbf{0} & \mathbf{K}_1 & \mathbf{K}_2 & -\mathbf{I} & \mathbf{0} & \mathbf{0} & \mathbf{0} & \mathbf{0} \\ \mathbf{0} & \mathbf{0} & \mathbf{0} & \mathbf{K}_3 & \mathbf{K}_2 & \mathbf{I} & \mathbf{0} & \mathbf{0} & \mathbf{0} & \mathbf{0} \\ \mathbf{0} & \mathbf{0} & \mathbf{0} & \mathbf{0} & \mathbf{K}_4 & \mathbf{K}_5 & \mathbf{K}_8 & \mathbf{K}_9 & \mathbf{0} & \mathbf{0} \\ \mathbf{0} & \mathbf{K}_{10} & \mathbf{K}_{11} & \mathbf{0} & \mathbf{K}_{12} & \mathbf{K}_{13} & \mathbf{K}_{14} & \mathbf{K}_{15} & \mathbf{0} & \mathbf{0} \\ \mathbf{0} & \mathbf{0} & \mathbf{0} & \mathbf{0} & \mathbf{0} & \mathbf{0} & \mathbf{K}_{16} & \mathbf{K}_{17} & \mathbf{K}_{18} & \mathbf{K}_{19} \\ \mathbf{0} & \mathbf{0} & \mathbf{0} & \mathbf{0} & \mathbf{0} & \mathbf{0} & \mathbf{K}_{20} & \mathbf{K}_{21} & \mathbf{K}_{22} & \mathbf{0} \\ \mathbf{0} & \mathbf{K}_{23} & \mathbf{K}_{24} & \mathbf{0} \end{bmatrix} \begin{bmatrix} \mathbf{A}_1 \\ \mathbf{A}_2 \\ \mathbf{B}_2 \\ \mathbf{C}_1 \\ \mathbf{C}_2 \\ \mathbf{D}_2 \\ \mathbf{A}_3 \\ \mathbf{B}_3 \\ \mathbf{B}_4 \\ \mathbf{D}_4 \end{bmatrix} = \begin{bmatrix} \mathbf{b}_1 \\ \mathbf{b}_3 \\ \mathbf{0} \\ \mathbf{b}_2 \\ \mathbf{b}_4 \\ \mathbf{0} \\ \mathbf{0} \\ \mathbf{0} \\ \mathbf{0} \\ \mathbf{0} \end{bmatrix} \quad (33)$$

where the column vectors of coefficients \mathbf{A}_1 , \mathbf{B}_1 , $\mathbf{C}_1 \sim \mathbf{D}_4$, $\mathbf{b}_1 \sim \mathbf{b}_4$ are constructed in the same way, e.g., $\mathbf{A}_1 = [A_{11}, A_{12}, \dots, A_{1N}]^T$, $\mathbf{A}_3 = [A_{31}, A_{32}, \dots, A_{3M}]^T$, $\mathbf{b}_1 = [b_{11}, b_{12}, \dots, b_{1N}]^T$. M , N are the maximum Fourier harmonic order. The definition of $\mathbf{K}_1 \sim \mathbf{K}_{22}$,

$b_1 \sim b_4$, and the detailed derivation process are shown in the Appendix. The integration constants can be obtained by solving the above equations.

IV. FORCE CALCULATION

According to the Maxwell stress theory, the force on a rigid body placed in the electromagnetic field can be calculated. The stress vector, i.e., the force per unit surface area, is given by [29-30]

$$\vec{f}_m = \frac{1}{\mu_0} \left(B_r^2 - \frac{1}{2} |\vec{B}|^2 \right) \vec{e}_r + \frac{1}{\mu_0} B_r B_\theta \vec{e}_\theta \quad (34)$$

As shown in (34), there are two components in the magnetic stress vector. One component is the radial component which can be used to calculate the radial force, that is, the y -direction force in the actual LPMSM, and the other is the tangential component which can be used to calculate the tangential force, that is, the x -direction force in the actual LPMSM. If it is assumed that the field is uniform along the axial direction, then the surface integration becomes a line integral multiplied by the axial length of iron core. The radial force and tangential force in the integral form can be written as

$$\vec{F}_r = \frac{1}{2\mu_0} L_1 \int_0^{2\pi} [B_{r2}^2(r, \theta) - B_{\theta2}^2(r, \theta)] r d\theta \quad (35)$$

$$\vec{F}_\theta = \frac{1}{\mu_0} L_1 \int_0^{2\pi} B_{r2}(r, \theta) B_{\theta2}(r, \theta) r d\theta \quad (36)$$

where L_1 is the axial length, r is the radius of the integration surface, B_{r2} and $B_{\theta2}$ are the radial and tangential components of the flux density at radius r , respectively.

Fig. 4 shows two different enclosed surfaces. One is the surface around the primary iron which is composed of 8 different surfaces that are located in Regions 2, 3 and 4, i.e., surfaces 1 and 5 located in Region 3, surfaces 2, 3, 4 located in Region 2. The force calculation will be very complicated. The other surface is a cylindrical surface entirely inside Region 2 which encloses the secondary back-iron and PMs in the analytical model. The total force acting on the primary iron is equal to that acting on the secondary back-iron and PMs except that their directions are opposite. The radius inside the air gap at which the integration surface is positioned is arbitrary, but for calculation purposes, it can be problematic if the surface is placed too close to the iron core surface. In this paper, a cylindrical surface is selected to calculate the force.

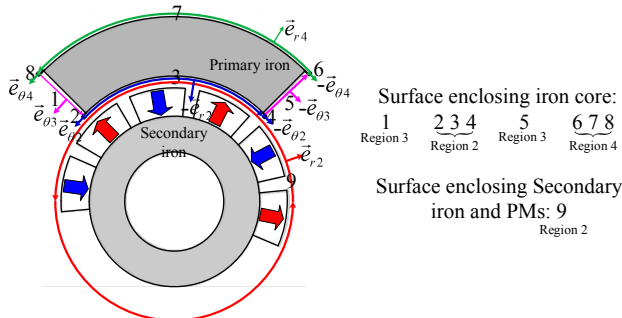


Fig. 4. The closed surface enclosing iron core and the closed surface enclosing back-iron and PMs.

V. VALIDATION BY FEM AND EXPERIMENT

To verify the analytical model, the linear FEM and non-linear FEM are both carried out on a LPMSM whose main parameters are shown in Table I. In linear FEM, the relative permeability of primary iron and secondary back-iron is 2000, and in non-linear FEM, the material of primary iron and secondary back-iron is steel_1010, which is used in the prototype. The corresponding parameters in approximate analytical models are shown in Table II. Based on the previous analysis in Section II, three different analytical models with different radius of curvature are listed. L_{re} is 500mm, 1000mm and 2000mm for machine 1, machine 2 and machine 3, respectively.

TABLE I
PARAMETERS OF LPMSM

Parameter	Value	Parameter	Value
Length of primary iron, L_s	50mm	Pole pitch, L_p	10mm
Height of primary iron, h_s	25mm	Width of PM, L_m	10mm
Length of secondary iron, L_r	210mm	Thickness of PM, h_m	4mm
Length of the end of secondary iron, L_e	5mm	Pole arc to pole pitch ratio, α_p	1.0
Axial length, L_1	50mm	Remanence of PM, B_r	1.27T
Length of air-gap, g	2mm	Relative permeability, μ_r	1.043
Number of PMs, N_p	20	Magnetization	Parallel

TABLE II
CORRESPONDING PARAMETERS IN ANALYTICAL MODEL OF LPMSM

Parameter	Machine 1	Machine 2	Machine 3
Extended length, L_{re}	500mm	1000mm	2000mm
Outer radius of PM, R_m	79.58mm	159.15mm	318.31mm
Span angle of primary iron, θ_1	36 deg	18 deg	9 deg
Inner radius of primary iron, R_s	81.58mm	161.15mm	320.31mm
Outer radius of primary iron, R_{so}	106.58mm	186.15mm	345.31mm
Outer radius of secondary iron, R_r	77.58 mm	155.15 mm	314.31 mm
Axial length, L_1	50 mm		
Length of air-gap, g	2 mm		
Pole pitch, θ_p	7.2 deg	3.6 deg	1.8 deg
Span angle of PM, θ_m	7.2 deg	3.6 deg	1.8 deg
Pole arc to pole pitch ratio, α_p	1.0		
Remanence of PM, B_r	1.27 T		
Relative permeability, μ_r	1.043		
Magnetization	Radial		

Fig. 5 shows the non-linear FEM predicted flux-line distributions when the primary iron is located at the middle position and at the end position, respectively. In order to clearly show the distribution, only the left part of LPMSM is displayed. Fig. 6 shows the analytically and FEM-predicted air-gap radial and tangential magnetic flux density distribution when the primary iron is located at the middle position. It can be seen that the nonlinearity of iron core has little impact on the magnetic field distribution due to the low saturation. And the predicted flux density obtained by the analytical model almost completely matches the FEM results. The matching degree increases with the increase of L_{re} . Fig. 7 shows the analytically and FEM predicted air-gap magnetic flux density distribution when the primary iron is located at the end position. The tangential force and normal force calculated by analytical model and FEM are shown in Fig. 8. Good agreement between the analytical results and FEM results can also be obtained.

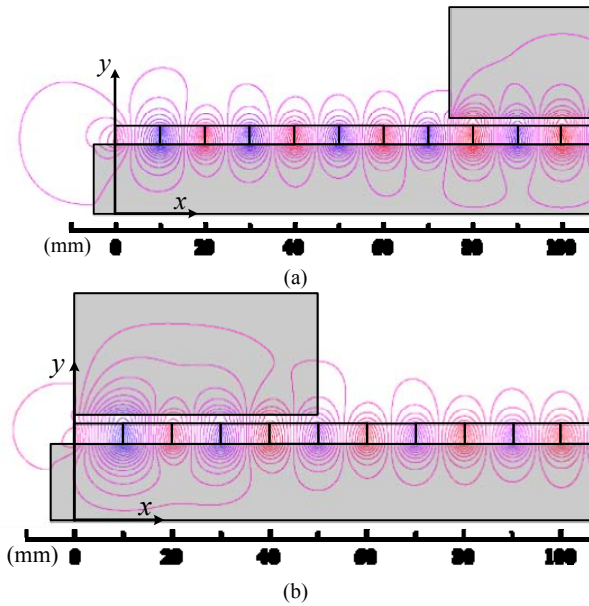


Fig. 5. Non-linear FEM predicted flux-line distribution with different relative position of primary iron and PMs. (a) Middle position; (b) End position.

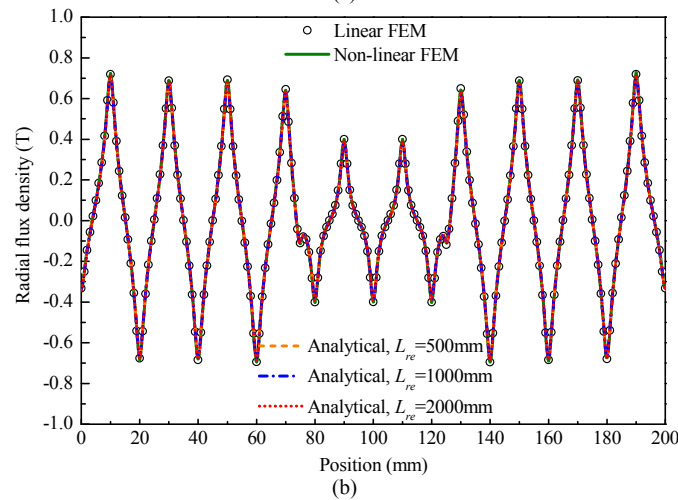
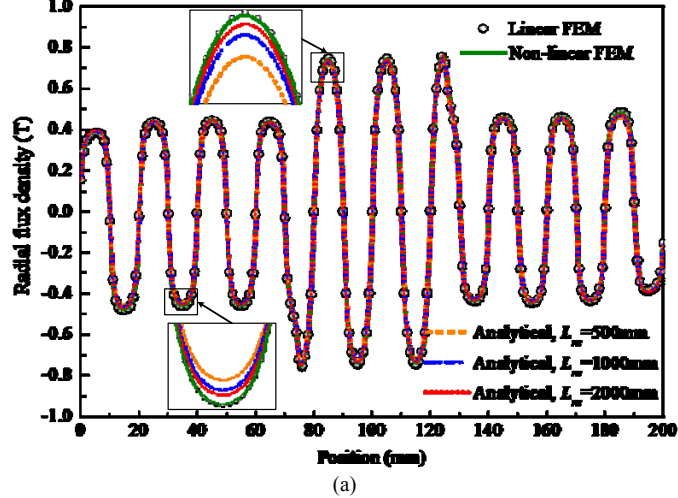


Fig. 6. Comparison of flux density at middle of the air gap when the primary iron is at the middle position: (a) Normal flux density; (b) Tangential flux density.

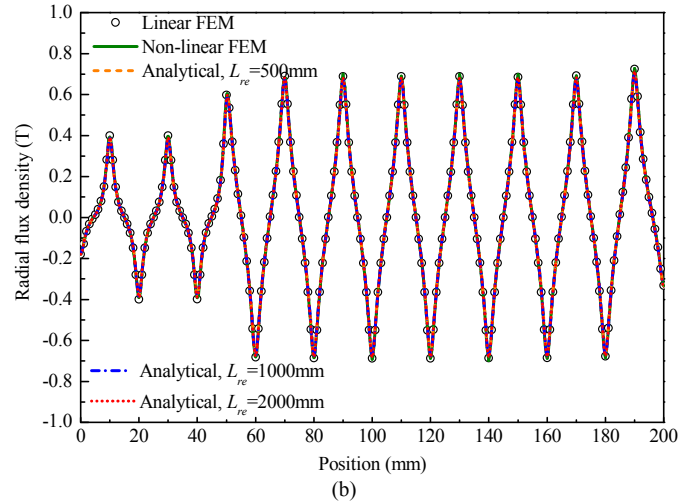
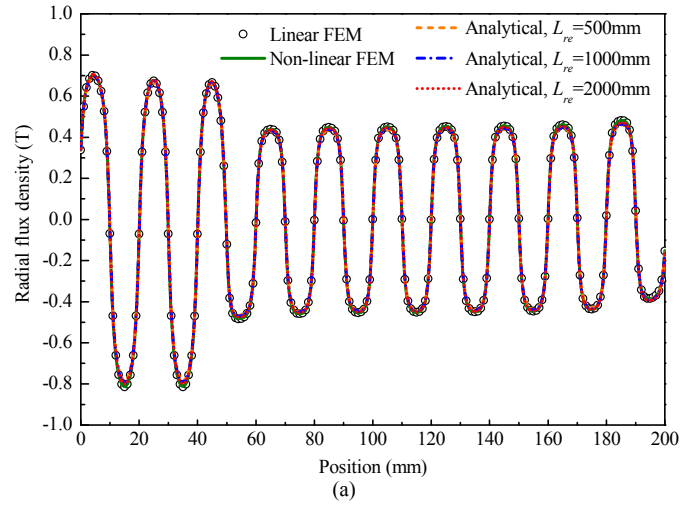
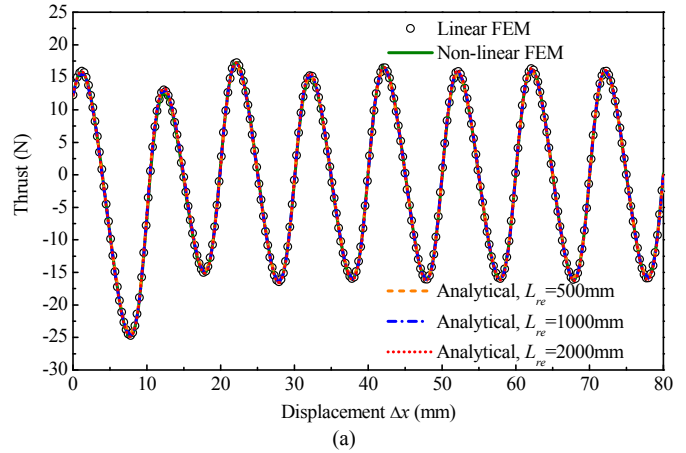


Fig. 7. Comparison of flux density at middle of the air gap when the primary iron is at the end position: (a) Normal flux density; (b) Tangential flux density.



(a)

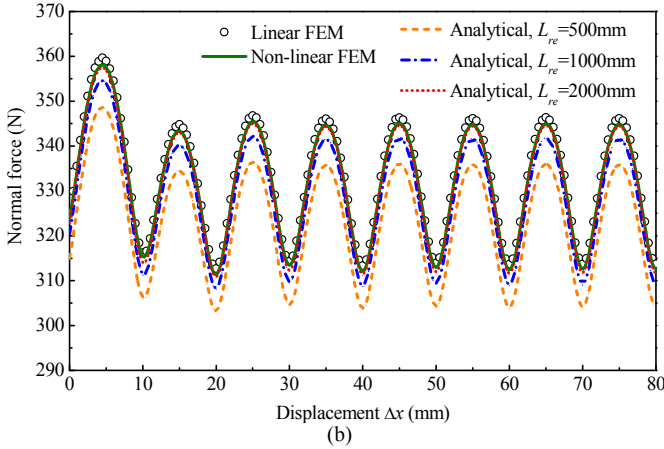


Fig. 8. Comparison of forces: (a) Thrust; (b) Normal force.

Meanwhile, the comparison of computation effort between the analytical method and FEM is also carried out. Considering the length of air-gap $g=2\text{mm}$, the maximum length of element in FEM is set as 0.8mm . In the approximate analytical model, the Fourier harmonic order M, N are both set as 400, 600, and 1000 for $L_{re}=500\text{mm}$, 1000mm , and 2000mm , respectively. This is mainly due to that with the increase of L_{re} , the pole pitch in analytical model decreases, as shown in Table II. The hardware sources of the computer for the analysis are CPU-3.80GHz and RAM-12.0GB. The computation times in static situation for different models are listed in Table III. It can be observed that: 1) the analytical method takes significantly less computation time than FEM; 2) the non-linear FEM takes more time than linear FEM due to the non-linear iteration; 3) in analytical model, with the increase of Fourier harmonic order, the computation time increases. For FEM, the computation time is mainly related to the number of mesh elements which is determined by the maximum length of element and the machine size. The finer meshes and the larger machine size will increase the computation time. However, for the analytical method, the computation time is determined by the number of subdomains and the Fourier harmonic order, and has no relation to the machine size. For example, if the length of LPMSM shown in Table I is 5 times longer, that is $L_r=1050\text{mm}$, the computation time of FEM will significantly increase. While the computation time of analytical model will have no change. On the other hand, if the pole pitch decreases, the computation time of analytical model will increase, while the computation time of FEM will have no change. Hence, the analytical method and FEM have their own features and originalities on computation effort.

TABLE III

COMPARISON OF COMPUTATION EFFORT BETWEEN THE ANALYTICAL METHOD AND FEM

Linear FEM	Non-linear FEM	Machine 1	Machine 2	Machine 3
1min58sec	2min50sec	2sec	6sec	20sec

To validate the analytical and FEM results of LPMSM, a slotless LPMSM prototype is manufactured and the experiment platform is built, as shown in Fig. 9. The thrust is measured by a force sensor with the fullscale of 98N and precision of 0.2% . The relative position between the primary iron and secondary back-iron is measured by a vernier caliper with precision of 0.02mm . Fig. 10 shows the comparison of tangential thrust

obtained by FEM, analytical model and experiment. Good agreement between the analytical results, and those obtained with FEM simulations and measured values verifies the validity of the proposed analytical model.

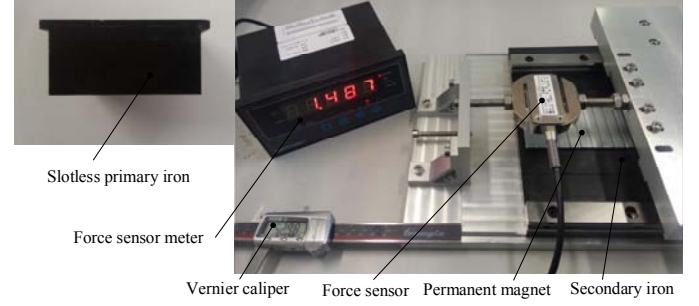


Fig. 9. The experiment platform for slotless LPMSM prototype.

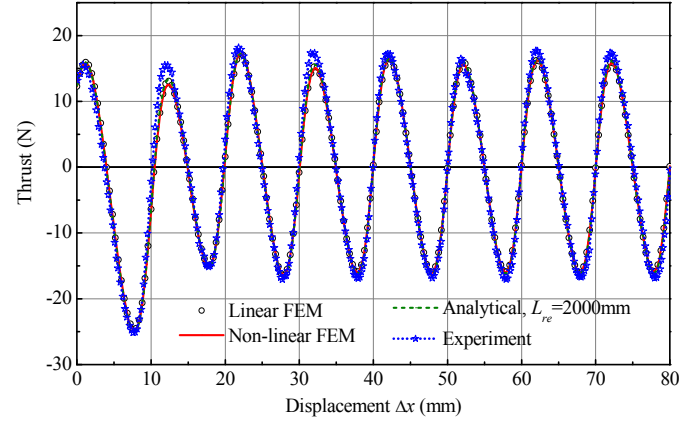


Fig. 10. Comparison of tangential thrust obtained by FEM, analytical and experiment.

VI. CONCLUSION

This paper has presented an analytical model for calculating the magnetic field and forces in the linear permanent-magnet synchronous machine. The analytical model is obtained by rolling the LPMSM into a rotary machine. In this model, the longitude end effect can be considered. The tangential thrust and normal forces are calculated by using Maxwell tensor theory. To validate the effectiveness of the proposed analytical model, FEM and experiments are both conducted. Excellent agreement is obtained between the analytical results, and the FEM and experimental results. The slot effect is neglected in this paper, but this model can deal with the slotted LPMSM with some modification, which will be done in the following research.

APPENDIX

1) Interface between Region 1 and Region 2

According to equations (15), (18), (19) and (27), the following equations can be obtained:

$$A_{1n} \left[1 + \left(\frac{R_r}{R_m} \right)^{2n} \right] - A_{2n} \left(\frac{R_m}{R_s} \right)^n - B_{2n} = b_{1n} \quad (37)$$

$$C_{1n} \left[1 + \left(\frac{R_r}{R_m} \right)^{2n} \right] - C_{2n} \left(\frac{R_m}{R_s} \right)^n - D_{2n} = b_{2n} \quad (38)$$

where

$$b_{1n} = -f_{1cn}(R_m)M_{\theta cn} + f_{1sn}(R_m)M_{r sn}$$

$$b_{2n} = -f_{1cn}(R_m)M_{\theta sn} - f_{1sn}(R_m)M_{r cn}$$

Equations (37)-(38) can be rewritten into matrix format as

$$\mathbf{K}_{1NN}\mathbf{A}_1 + \mathbf{K}_{2NN}\mathbf{A}_2 - \mathbf{I}_{NN}\mathbf{B}_2 = \mathbf{b}_1 \quad (39)$$

$$\mathbf{K}_{1NN}\mathbf{C}_1 + \mathbf{K}_{2NN}\mathbf{C}_2 - \mathbf{I}_{NN}\mathbf{D}_2 = \mathbf{b}_2 \quad (40)$$

where

$$\mathbf{K}_{1NN} = \text{diag} \left(1 + \left(\frac{R_r}{R_m} \right)^2, 1 + \left(\frac{R_r}{R_m} \right)^4, \dots, 1 + \left(\frac{R_r}{R_m} \right)^{2N} \right)_{N \times N}$$

$$\mathbf{K}_{2NN} = \text{diag} \left(-\left(\frac{R_m}{R_s} \right)^1, -\left(\frac{R_m}{R_s} \right)^2, \dots, -\left(\frac{R_m}{R_s} \right)^N \right)_{N \times N}$$

$$\mathbf{I}_{NN} = \text{diag}(1, 1, \dots, 1)_{N \times N}$$

And according to equations (15), (18), (19) and (28), the following equations can be obtained:

$$A_{1n} \frac{1}{\mu_r} \left[1 - \left(\frac{R_r}{R_m} \right)^{2n} \right] - A_{2n} \left(\frac{R_m}{R_s} \right)^n + B_{2n} = b_{3n} \quad (41)$$

$$C_{1n} \frac{1}{\mu_r} \left[1 - \left(\frac{R_r}{R_m} \right)^{2n} \right] - C_{2n} \left(\frac{R_m}{R_s} \right)^n + D_{2n} = b_{4n} \quad (42)$$

where

$$b_{3n} = -\frac{R_m}{n\mu_r} \left\{ \left[g_{1cn}(R_m) + \mu_0 \right] M_{c\theta n} - g_{1sn}(R_m) M_{srn} \right\}$$

$$b_{4n} = -\frac{R_m}{n\mu_r} \left\{ \left[g_{1cn}(R_m) + \mu_0 \right] M_{s\theta n} + g_{1sn}(R_m) M_{crn} \right\}$$

$$g_{1cn}(r) = \begin{cases} \frac{\mu_0}{n^2-1} \left[-\left(n \right)^2 \left(\frac{R_r}{r} \right)^{n+1} + 1 \right] & n \neq 1 \\ \frac{\mu_0}{2} \left[-(1 - \ln R_r) \left(\frac{R_r}{r} \right)^2 - \ln r - 1 \right] & n = 1 \end{cases}$$

$$g_{1sn}(r) = \begin{cases} \frac{\mu_0}{n^2-1} \left[-n \left(\frac{R_r}{r} \right)^{n+1} + n \right] & n \neq 1 \\ -\frac{\mu_0}{2} \left[-(1 + \ln R_r) \left(\frac{R_r}{r} \right)^2 + \ln r + 1 \right] & n = 1 \end{cases}$$

Equations (41)-(42) can be rewritten as

$$\mathbf{K}_{3NN}\mathbf{A}_1 + \mathbf{K}_{2NN}\mathbf{A}_2 + \mathbf{I}_{NN}\mathbf{B}_2 = \mathbf{b}_3 \quad (43)$$

$$\mathbf{K}_{3NN}\mathbf{C}_1 + \mathbf{K}_{2NN}\mathbf{C}_2 + \mathbf{I}_{NN}\mathbf{D}_2 = \mathbf{b}_4 \quad (44)$$

where

$$\mathbf{K}_{3NN} = \frac{1}{\mu_r} \times \text{diag} \left(1 - \left(\frac{R_r}{R_m} \right)^2, 1 - \left(\frac{R_r}{R_m} \right)^4, \dots, 1 - \left(\frac{R_r}{R_m} \right)^{2N} \right)_{N \times N}$$

2) Interface between Region 2 and Region 3

The tangential field strength in Region 3 is given by

$$H_{\theta 3} = \frac{1}{\mu_0} \sum_{m=1}^{\infty} \left[A_{3m} f_{3cm}(r) + B_{3m} g_{3m}(r) \right] \cos \frac{m\pi}{\theta_2} \left(\theta_s + \frac{\theta_2}{2} - \pi \right) \quad (45)$$

where

$$f_{3m}(r) = -\frac{m\pi}{\theta_2} \frac{1}{R_{so}} \left(\frac{r}{R_{so}} \right)^{\frac{m\pi}{\theta_2}-1} \quad \text{and} \quad g_{3m}(r) = \frac{m\pi}{\theta_2} \frac{1}{R_s} \left(\frac{r}{R_s} \right)^{-\frac{m\pi}{\theta_2}-1}$$

By assuming

$$H_{\theta 3} \Big|_{r=R_s} = 0 \quad \theta_s \in \left(\pi + \frac{\theta_2}{2}, 2\pi \right) \cup \left(0, \pi - \frac{\theta_2}{2} \right) \quad (46)$$

The tangential field strength can be expanded into Fourier series in $0 \sim 2\pi$:

$$H_{\theta 3}^s = \sum_{n=1}^{\infty} A_{Sn} \cos(n\theta_s) + B_{Sn} \sin(n\theta_s) \quad (47)$$

where

$$A_{Sn} = \frac{1}{\pi} \int_0^{2\pi} H_{\theta 3} \cos(n\theta_s) d\theta_s$$

$$= \sum_{m=1}^{\infty} \left[A_{3m} f_{3cam}(r) + B_{3m} f_{3cbm}(r) \right] \eta(m, n)$$

$$B_{Sn} = \sum_{m=1}^{\infty} \left[A_{3m} f_{3cam}(r) + B_{3m} f_{3cbm}(r) \right] \xi(m, n)$$

$$\eta(m, n) = \frac{-n\theta_2^2 \cos m\pi \sin n \left(\frac{\theta_2}{2} + \pi \right) - \sin n \left(-\frac{\theta_2}{2} + \pi \right)}{\mu_0 \pi \left((m\pi)^2 - (n\theta_2)^2 \right)} \quad n\theta_2 \neq m\pi$$

$$\eta(m, n) = \frac{\theta_2}{2\mu_0 \pi} \cos \left[\frac{m\pi}{\theta_2} \left(\frac{\theta_2}{2} - \pi \right) \right]$$

$$+ \frac{1}{4n\mu_0 \pi} \left[\cos m\pi \sin n \left(\frac{\theta_2}{2} + \pi \right) - \sin n \left(-\frac{\theta_2}{2} + \pi \right) \right] \quad n\theta_2 = m\pi$$

$$\xi(m, n) = \frac{n\theta_2^2 \cos m\pi \cos n \left(\frac{\theta_2}{2} + \pi \right) - \cos n \left(-\frac{\theta_2}{2} + \pi \right)}{\mu_0 \pi \left((m\pi)^2 - (n\theta_2)^2 \right)} \quad n\theta_2 \neq m\pi$$

$$\xi(m, n) = \frac{\theta_2}{2\mu_0 \pi} \sin \left[\frac{m\pi}{\theta_2} \left(-\frac{\theta_2}{2} + \pi \right) \right]$$

$$- \frac{1}{4n\mu_0 \pi} \left[\cos m\pi \cos n \left(\frac{\theta_2}{2} + \pi \right) - \cos n \left(-\frac{\theta_2}{2} + \pi \right) \right] \quad n\theta_2 = m\pi$$

Then, according to equations (15), (19), and (30), the following equation set can be obtained:

$$-A_{2n} \frac{n}{R_s} + B_{2n} \frac{n}{R_s} \left(\frac{R_m}{R_s} \right)^n = \sum_{m=1}^{\infty} A_{3m} f_{3m}(R_s) \eta(m, n)$$

$$+ \sum_{m=1}^{\infty} B_{3m} g_{3m}(R_s) \eta(m, n) \quad (48)$$

$$-C_{2n} \frac{n}{R_s} + D_{2n} \frac{n}{R_s} \left(\frac{R_m}{R_s} \right)^n = \sum_{m=1}^{\infty} A_{3m} f_{3m}(R_s) \xi(m, n)$$

$$+ \sum_{m=1}^{\infty} B_{3m} g_{3m}(R_s) \xi(m, n) \quad (49)$$

Equations (48)-(49) can be rewritten as

$$\mathbf{K}_{4NN}\mathbf{A}_2 + \mathbf{K}_{5NN}\mathbf{B}_2 + \mathbf{K}_{6NM}\mathbf{A}_3 + \mathbf{K}_{7NM}\mathbf{B}_3 = \mathbf{0} \quad (50)$$

$$\mathbf{K}_{4NN}\mathbf{C}_2 + \mathbf{K}_{5NN}\mathbf{D}_2 + \mathbf{K}_{8NM}\mathbf{A}_3 + \mathbf{K}_{9NM}\mathbf{B}_3 = \mathbf{0} \quad (51)$$

where

$$\mathbf{K}_{4NN} = \text{diag} \left(\frac{1}{R_s}, \frac{2}{R_s}, \dots, \frac{N}{R_s} \right)_{N \times N}$$

$$\mathbf{K}_{5NN} = \text{diag} \left(\frac{R_m}{R_s^2}, \frac{2R_m^2}{R_s^3}, \dots, \frac{N}{R_s} \left(\frac{R_m}{R_s} \right)^N \right)_{N \times N}$$

$$\mathbf{K}_{6NM} = \boldsymbol{\eta}_{MN}^T \mathbf{F}_{1MM} \quad \mathbf{K}_{7NM} = \boldsymbol{\eta}_{MN}^T \mathbf{G}_{1MM} \quad \mathbf{K}_{8NM} = \boldsymbol{\xi}_{MN}^T \mathbf{F}_{1MM}$$

$$\mathbf{K}_{9NM} = \boldsymbol{\xi}_{MN}^T \mathbf{G}_{1MM}$$

$$\begin{aligned} \mathbf{F}_{1MM} &= \text{diag}(f_{31}(R_s), f_{32}(R_s), \dots, f_{3M}(R_s))_{M \times M} \\ \mathbf{G}_{1MM} &= \text{diag}(g_{31}(R_s), g_{32}(R_s), \dots, g_{3M}(R_s))_{M \times M} \\ \boldsymbol{\eta}_{MN} &= (\eta(m, n))_{M \times N} \quad \boldsymbol{\xi}_{MN} = (\xi(m, n))_{M \times N} \end{aligned}$$

The vector potential expression in Region 2 can be expanded into Fourier series over the interface:

$$A_{z2}^s = \sum_{m=1}^{\infty} E_{2m} \cos \frac{m\pi}{\theta_2} \left(\theta_s + \frac{\theta_2}{2} - \pi \right) \quad \theta_s \in \left(\pi - \frac{\theta_2}{2}, \pi + \frac{\theta_2}{2} \right) \quad (52)$$

where

$$\begin{aligned} E_{2m} &= \sum_{n=1}^{\infty} \left[A_{2n} \left(\frac{r}{R_s} \right)^n + B_{2n} \left(\frac{r}{R_m} \right)^{-n} \right] \frac{2\pi}{\theta_2} \eta(m, n) \\ &+ \sum_{n=1}^{\infty} \left[C_{2n} \left(\frac{r}{R_s} \right)^n + D_{2n} \left(\frac{r}{R_m} \right)^{-n} \right] \frac{2\pi}{\theta_2} \xi(m, n) \end{aligned}$$

According to equations (23), (29) and (52), the following equation can be obtained:

$$A_{3m} \left(\frac{r}{R_{so}} \right)^{\frac{m\pi}{\theta_2}} + B_{3m} \left(\frac{r}{R_s} \right)^{\frac{m\pi}{\theta_2}} = E_{2m} \quad (53)$$

Equation (53) can be rewritten as

$$\mathbf{K}_{10MN} \mathbf{A}_2 + \mathbf{K}_{11MN} \mathbf{B}_2 + \mathbf{K}_{12MN} \mathbf{C}_2 + \mathbf{K}_{13MN} \mathbf{D}_2 + \mathbf{K}_{14MM} \mathbf{A}_3 + \mathbf{K}_{15MM} \mathbf{B}_3 = \mathbf{0} \quad (54)$$

where

$$\mathbf{K}_{10MN} = \boldsymbol{\eta}_{MN} \mathbf{F}_{2NN} \quad \mathbf{K}_{11MN} = \boldsymbol{\eta}_{MN} \mathbf{G}_{2NN} \quad \mathbf{K}_{12MN} = \boldsymbol{\xi}_{MN} \mathbf{F}_{2NN}$$

$$\mathbf{K}_{13MN} = \boldsymbol{\xi}_{MN} \mathbf{G}_{2NN}$$

$$\mathbf{K}_{14MM} = -\text{diag} \left(\left(\frac{R_s}{R_{so}} \right)^{\frac{\pi}{\theta_2}}, \left(\frac{R_s}{R_{so}} \right)^{\frac{2\pi}{\theta_2}}, \dots, \left(\frac{R_s}{R_{so}} \right)^{\frac{M\pi}{\theta_2}} \right)$$

$$\mathbf{K}_{15MM} = -\text{diag}(1, 1, \dots, 1) \quad \mathbf{F}_{2NN} = \frac{2\pi}{\theta_2} \times \text{diag}(1, 1, \dots, 1)_{N \times N}$$

$$\mathbf{G}_{2NN} = \frac{2\pi}{\theta_2} \times \text{diag} \left(\left(\frac{r}{R_m} \right)^{-1}, \left(\frac{r}{R_m} \right)^{-2}, \dots, \left(\frac{r}{R_m} \right)^{-N} \right)_{N \times N}$$

3) Interface between Region 3 and Region 4

According to equations (15), (26), (32), and (47), the following equation set can be obtained:

$$B_{4n} \frac{n}{R_{so}} = \sum_{m=1}^{\infty} \left[A_{3m} f_{3m}(R_{so}) + B_{3m} g_{3m}(R_{so}) \right] \eta(m, n) \quad (55)$$

$$D_{4n} \frac{n}{R_{so}} = \sum_{m=1}^{\infty} \left[A_{3m} f_{3m}(R_{so}) + B_{3m} g_{3m}(R_{so}) \right] \xi(m, n) \quad (56)$$

Equations (55)-(56) can be rewritten as

$$\mathbf{K}_{20NM} \mathbf{A}_3 + \mathbf{K}_{21NM} \mathbf{B}_3 + \mathbf{K}_{22NN} \mathbf{B}_4 = \mathbf{0} \quad (57)$$

$$\mathbf{K}_{23NM} \mathbf{A}_3 + \mathbf{K}_{24NM} \mathbf{B}_3 + \mathbf{K}_{22NN} \mathbf{D}_4 = \mathbf{0} \quad (58)$$

where

$$\mathbf{K}_{20NM} = \boldsymbol{\eta}_{MN}^T \mathbf{F}_{3MM} \quad \mathbf{K}_{21NM} = \boldsymbol{\eta}_{MN}^T \mathbf{G}_{3MM} \quad \mathbf{K}_{23NM} = \boldsymbol{\xi}_{MN}^T \mathbf{F}_{3MM}$$

$$\mathbf{K}_{24NM} = \boldsymbol{\xi}_{MN}^T \mathbf{G}_{3MM}$$

$$\mathbf{K}_{22NN} = \text{diag} \left(\frac{1}{R_{so}}, \frac{2}{R_{so}}, \dots, \frac{N}{R_{so}} \right)_{N \times N}$$

$$\mathbf{F}_{3MM} = \text{diag}(f_{31}(R_{so}), f_{32}(R_{so}), \dots, f_{3M}(R_{so}))_{M \times M}$$

$$\mathbf{G}_{3MM} = \text{diag}(g_{31}(R_{so}), g_{32}(R_{so}), \dots, g_{3M}(R_{so}))_{M \times M}$$

The vector potential expression in Region 4 can be expanded into Fourier series over the interface:

$$A_{z4}^s = \sum_{m=1}^{\infty} E_{4m} \cos \frac{m\pi}{\theta_2} \left(\theta_s + \frac{\theta_2}{2} - \pi \right) \quad \theta_s \in \left(\pi - \frac{\theta_2}{2}, \pi + \frac{\theta_2}{2} \right) \quad (59)$$

where

$$E_{4m} = \frac{2\pi}{\theta_2} \sum_{n=1}^{\infty} B_{4n} \left(\frac{r}{R_{so}} \right)^{-n} \eta(m, n) + D_{4n} \left(\frac{r}{R_{so}} \right)^{-n} \xi(m, n)$$

According to equations (26), (31) and (59), the following equation can be obtained:

$$A_{3m} \left(\frac{r}{R_{so}} \right)^{\frac{m\pi}{\theta_2}} + B_{3m} \left(\frac{r}{R_s} \right)^{\frac{m\pi}{\theta_2}} = E_{4m} \quad (60)$$

Equation (60) can be rewritten as

$$\mathbf{K}_{16MM} \mathbf{A}_3 + \mathbf{K}_{17MM} \mathbf{B}_3 + \mathbf{K}_{18MN} \mathbf{B}_4 + \mathbf{K}_{19MN} \mathbf{D}_4 = \mathbf{0} \quad (61)$$

where

$$\mathbf{K}_{16MM} = -\text{diag}(1, 1, \dots, 1)$$

$$\mathbf{K}_{17MM} = -\text{diag} \left(\left(\frac{R_{so}}{R_s} \right)^{-\frac{\pi}{\theta_2}}, \left(\frac{R_{so}}{R_s} \right)^{-\frac{2\pi}{\theta_2}}, \dots, \left(\frac{R_{so}}{R_s} \right)^{-\frac{M\pi}{\theta_2}} \right)$$

$$\mathbf{K}_{18MN} = \boldsymbol{\eta}_{MN} \mathbf{F}_{4NN} \quad \mathbf{K}_{19MN} = \boldsymbol{\xi}_{MN} \mathbf{F}_{4NN}$$

$$\mathbf{F}_{4NN} = \frac{2\pi}{\theta_2} \times \text{diag}(1, 1, \dots, 1)_{N \times N}$$

Finally, equations (39)-(40), (43)-(44), (50)-(51), (54), (57)-(58), and (61) lead to the matrix equation as shown in (33).

REFERENCES

- [1] R. W. Cao, M. Cheng, C. C. Mi, and W. Hua, "Influence of leading design parameters on the force performance of a complementary and modular linear flux-switching permanent-magnet motor," *IEEE Trans. Ind. Electron.*, vol. 61, no. 5, pp. 2165-2175, May 2014.
- [2] M. Y. Wang, L. Y. Li, and D. H. Pan, "Detent force compensation for PMLSM systems based on structural design and control method combination," *IEEE Trans. Ind. Electron.*, vol. 62, no. 11, pp. 6845-6854, Nov. 2015.
- [3] J. H. Ji, S. J. Yan, W. X. Zhao, G. H. Liu, and X. Y. Zhu, "Minimization of cogging force in a novel linear permanent-magnet motor for artificial hearts," *IEEE Trans. Magn.*, vol. 49, no. 7, pp. 3901-3904, July 2013.
- [4] M. Y. Wang, L. Y. Li, and D. H. Pan, "Analytical modeling and design optimization of linear synchronous motor with stair-step-shaped magnetic poles for electromagnetic launch applications," *IEEE Trans. Plasma Sci.*, vol. 40, no. 2, pp. 519-527, Feb. 2012.
- [5] L. Cappelli, Y. Coia, F. Marignetti, and Z. Q. Zhu, "Analysis of eccentricity in permanent-magnet tubular machines," *IEEE Trans. Ind. Electron.*, vol. 61, no. 5, pp. 2208-2216, May 2014.
- [6] F. Cupertino, P. Giangrande, G. Pellegrino, and L. Salvatore, "End effects in linear tubular motors and compensated position sensorless control based on pulsating voltage injection," *IEEE Trans. Ind. Electron.*, vol. 61, no. 5, pp. 2208-2216, May 2014.
- [7] O. Danielsson and M. Leijon, "Flux distribution in linear permanent-magnet synchronous machines including longitudinal end effects," *IEEE Trans. Magn.*, vol. 43, no. 7, pp. 3197-3201, July 2007.
- [8] G. Lei, T. S. Wang, Y. G. Guo, J. G. Zhu, and S. H. Wang, "System-level design optimization methods for electrical drive systems: deterministic approach," *IEEE Trans. Ind. Electron.*, vol. 61, no. 12, pp. 6591-6602, Dec. 2014.
- [9] G. Lei, T. S. Wang, Y. G. Guo, J. G. Zhu, and S. H. Wang, "System-level design optimization method for electrical drive systems-robust approach," *IEEE Trans. Ind. Electron.*, vol. 62, no. 8, pp. 4702-4713, Aug. 2015.

- [10] Y. J. Kim, M. Watada, and H. Dohmeki, "Reduction of the cogging force at the outlet edge of a stationary discontinuous primary linear synchronous motor," *IEEE Trans. Magn.*, vol. 43, no. 1, pp. 40-45, Jan. 2007.
- [11] Y. M. Chen, S. Y. Fan, and W. S. Lu, "Performance analysis of linear permanent-magnet motors with finite-element analysis," *IEEE Trans. Magn.*, vol. 44, no. 3, pp. 377-385, Mar. 2008.
- [12] I. C. Vese, F. Marignetti, and M. M. Radulescu, "Multiphysics approach to numerical modeling of a permanent-magnet tubular linear motor," *IEEE Trans. Ind. Electron.*, vol. 57, no. 1, pp. 320-326, Jan. 2010.
- [13] M. N. Ma, L. Y. Li, Z. He, and C. C. Chan, "Influence of longitudinal end-effects on electromagnetic performance of a permanent magnet slotless linear launcher," *IEEE Trans. Plasma Sci.*, vol. 43, no. 5, pp. 1161-1166, May. 2013.
- [14] C. Pompermaier, K. F. J. Haddad, A. Zambonetti, M. V. Ferreira da Luz, and I. Boldea, "Small linear PM oscillatory motor: magnetic circuit modeling corrected by axisymmetric 2-D FEM and experimental characterization," *IEEE Trans. Ind. Electron.*, vol. 59, no. 3, pp. 1189-1196, Mar. 2012.
- [15] K. Sato, "Thrust ripple reduction in ultrahigh-acceleration moving-permanent-magnet linear synchronous motor," *IEEE Trans. Magn.*, vol. 48, no. 12, pp. 4866-4873, Dec. 2012.
- [16] S. Vaez-Zadeh and A. Hassanpour Isfahani, "Enhanced modeling of linear permanent-magnet synchronous motors," *IEEE Trans. Magn.*, vol. 43, no. 1, pp.33-39, Jan. 2007.
- [17] B. Sheikh-Ghalavand, S. Vaez-Zadeh, and A. Hassanpour Isfahani, "An improved magnetic equivalent circuit model for iron-core linear permanent-magnet synchronous motors," *IEEE Trans. Magn.*, vol. 46, no. 1, pp. 112-120, Jan. 2010.
- [18] A. Souissi, M. W. Zouaghi, I. Abdennadher, and A. Masmoudi, "MEC-based modeling and sizing of a tubular linear PM synchronous machine," *IEEE Trans. Ind. Appl.*, vol. 51, no. 3, pp. 2181-2194, May/June 2015.
- [19] X. Chen and Z. Q. Zhu, "Analytical determination of optimal split ratio of E-core permanent magnet linear oscillating actuators," *IEEE Trans. Ind. Appl.*, vol. 47, no. 1, pp. 25-33, Jan./Feb. 2011.
- [20] A. H. Isfahani, "Analytical framework for thrust enhancement in permanent-magnet (PM) linear synchronous motors with segmented PM poles," *IEEE Trans. Magn.*, vol. 46, no. 4, pp. 1116-1122, Apr. 2010.
- [21] J. B. Wang, G. W. Jewell, and D. Howe, "Analytical framework for thrust enhancement in permanent-magnet (PM) linear synchronous motors with segmented PM poles," *IEEE Trans. Magn.*, vol. 35, no. 3, pp. 1986-2000, May 1999.
- [22] Y. Amara and G. Barakat, "Analytical modeling of magnetic field in surface mounted permanent-magnet tubular linear machines," *IEEE Trans. Magn.*, vol. 46, no. 11, pp. 3870-3884, Nov. 2010.
- [23] L. Yan, L. Zhang, Z. X. Jiao, H. J. Hu, C. Y. Chen, and I-Ming Chen, L. Z. Zeng, X. D. Chen, X. Q. Li, W. Jiang, and X. Luo, "Armature reaction field and inductance of coreless moving-coil tubular linear machine," *IEEE Trans. Ind. Electron.*, vol. 61, no. 12, pp. 6956-6965, Dec. 2014.
- [24] T. T. Overboom, J. P. C. Smeets, J.W. Jansen, and E. A. Lomonova, "Semianalytical calculation of the torque in a linear permanent-magnet motor with finite yoke length," *IEEE Trans. Magn.*, vol. 48, no. 11, pp. 3575-3578, Nov. 2012.
- [25] X. D. Wang, P. L. Wang, and X. Z. Xu, "Magnetic field analytical calculation of the permanent magnet synchronous linear motor with fractional slot concentrated windings," in *Proc. ICEMS*, Oct. 2014, pp. 1762-1767.
- [26] Y. Laoubi, M. Dhifli, G. Verez, Y. Amara, and G. Barakat, "Open circuit performance analysis of a permanent magnet linear machine using a new hybrid analytical model," *IEEE Trans. Magn.*, vol. 51, no. 3, art. 8102304, Mar. 2015.
- [27] L. Z. Zeng, X. D. Chen, X. Q. Li, W. Jiang, and X. Luo, "A thrust force analysis method for permanent magnet linear motor using Schwarz-Christoffel mapping and considering slotting effect, end effect, and magnet Shape," *IEEE Trans. Magn.*, vol. 51, no. 9, art. 8107609, Sep. 2015.
- [28] Z. Q. Zhu, D. Howe, E. Bolte, and B. Ackermann, "Instantaneous magnetic field distribution in brushless permanent magnet dc motors, part I: open-circuit field," *IEEE Trans. Magn.*, vol. 29, no. 1, pp. 124-135, Jan. 1993.
- [29] D. Zarko, D. Ban, and T. A. Lipo, "Analytical solution for cogging torque in surface permanent-magnet motors using conformal mapping," *IEEE Trans. Magn.*, vol. 44, no.1, pp. 52-65, Jan. 2008.
- [30] Y. Zhou, H. S. Li, G. W. Meng, S. Zhou, and Q. Cao, "Analytical calculation of magnetic field and cogging torque in surface-mounted permanent-magnet accounting for any eccentric rotor shape," *IEEE Trans. Ind. Electron.*, vol. 62, no. 6, pp. 3438-3447, Jun. 2015.